Journal of Physics D: Applied Physics

Check for updates

OPEN ACCESS

RECEIVED
12 December 2025

REVISED
6 February 2026

ACCEPTED FOR PUBLICATION
24 February 2026

PUBLISHED
9 March 2026

Original content from this work may be used under the terms of the Creative Commons Attribution 4.0 licence.

Any further distribution of this work must maintain attribution to the author(s) and the title of the work, journal citation and DOI.

PAPER

In-situ determination of the effective secondary electron emission coefficient in helium and neon capacitively coupled RF plasmas

Ranna Masheyeva[1,*], Aranka Derzsi[1], Karlygash Dzhumagulova[2], Murat Myrzaly[2,3], Zoltán Donkó[1] and Peter Hartmann[1]

[1] Institute for Solid State Physics and Optics, HUN-REN Wigner Research Centre for Physics, 1121 Budapest, Hungary
[2] Research Institute of Experimental and Theoretical Physics, Al-Farabi Kazakh National University, 050040 Almaty, Kazakhstan
[3] Department of General Physics, Satbayev University, 050013 Almaty, Kazakhstan
[*] Author to whom any correspondence should be addressed.

E-mail: masheyeva.ranna@gmail.com

Keywords: low-pressure radio frequency discharges, capacitive coupling, electrical asymmetry effect, kinetic plasma modeling, electron emission

Abstract

Building on our previous study in argon gas, we extend our approach to helium and neon capacitively coupled plasmas, which allows the effective secondary-electron emission coefficient (SEEC, γ) to be determined *in-situ* under discharge operation. The method relies on the γ-dependence of the DC self-bias voltage, which arises due to the electrical asymmetry effect (EAE). The EAE is induced by applying two consecutive radio-frequency harmonics with a variable phase angle to excite the discharge. Experimental measurements of the DC self-bias voltage are complemented by particle-in-cell/Monte Carlo collisions simulations. A sequence of SEEC values is used in the simulations, and the actual γ is determined by matching the computed DC self-bias to the experimental value. Applying this method at a driving frequency of 4 MHz, we obtain effective γ values of 0.105 and 0.165 for helium at 120 Pa and 240 Pa, respectively, and 0.072 and 0.103 for neon at 80 Pa and 160 Pa, respectively, with an estimated uncertainty of ± 0.01.

1. Introduction

Surface processes play a key role in determining the characteristics of capacitively coupled plasmas (CCPs) used in a variety of technological applications [1–4]. In these applications, plasma particles interact with electrode surfaces, altering surface conditions, while surface processes can in turn significantly modify discharge properties. A detailed understanding of such plasma-surface interactions is therefore essential for the development and optimization of plasma-based technologies. Noble-gas discharges, including those in helium and neon, are widely used in plasma processing and are extensively studied using various plasma diagnostic techniques. For example, helium and neon ion beams have been employed for precise nanoscale etching and repair of resist patterns [5], as well as for the modification of multilayer structures in nanofabrication [6] and for extreme ultraviolet lithography [7]. In addition to these, noble-gas plasmas are also utilized in thin-film growth, surface modification processes [8], and in ultraviolet and extreme-ultraviolet radiation sources [9].

One of the crucial parameters governing plasma–surface interactions is the effective secondary electron emission coefficient (SEEC), γ, which accounts for the emission of electrons from electrode surfaces induced by various incident species. In CCPs, these incident species include ions, metastable atoms, fast neutrals, and photons, all of which may contribute to the generation of so-called γ-electrons [10, 11]. Electrons themselves can also trigger secondary emission, producing the so-called δ-electrons [12, 13]. Under certain conditions, these secondary electrons can initiate ionization avalanches within the sheath region, thereby substantially increasing the plasma density [14–16]. The presence of electronically excited atoms was found to amplify this effect even further due to excited-state neutral- and photon-induced SEE on electrode surfaces [15]. Radmilovic-Radjenovic *et al* [17, 18] demonstrated the importance of these effects for RF breakdown in argon, while Braginsky *et al* [19] showed that

© 2026 The Author(s). Published by IOP Publishing Ltd

in low-frequency RF discharges with high applied voltages, ion- and fast-atom-induced SEE plays an important role in sustaining the discharge and in maintaining power balance. At intermediate pressures, Gudmundsson *et al* [20] reported that secondary electrons strongly contribute to transitions between discharge modes. Complementary computational studies by Liu *et al* [21] revealed strong plasma-density enhancement. The effect of ion-induced SEE on electronegative oxygen plasmas was demonstrated by Proto and Gudmundsson [22] showing increase of the electron density and reduction of the electronegativity. Furthermore, recent studies have shown that SEE can control ion properties in dual- and multi-frequency CCPs [23], modify electron heating in RF hollow cathodes [24], and together with surface charging, influence high-aspect-ratio etching processes [25]. In addition, the influence of electron-induced SEE has been associated with multipactor development driven by secondary emission and space-charge effects [26], changes in sheath dynamics [27], plasma–dielectric interaction and electron reflection [28], the suppression or triggering of multipactor processes [29], and, in multipactor-induced plasma ionisation breakdown, higher-harmonic field generation arising from stream–plasma instabilities [30].

The minimum energy required to remove an electron from a solid surface, known as the work function, can be supplied either by electrostatic potential energy or by the kinetic energy of an impacting ion [31, 32]. Under typical CCP operating conditions—moderate pressures and voltages—the contribution from kinetic electron emission is generally negligible, and ion–neutral collisions typically do not generate fast neutrals with sufficient energy to significantly enhance secondary electron emission. So, the combined effect of ion-, metastable-, and photon-induced emission are commonly represented by an effective ion induced SEEC, γ [1, 11], which provides a practical representation of the total emission yield relevant to the discharge environment. As discussed above, the γ coefficient has a significant impact on plasma characteristics, therefore, its accurate determination remains crucial for reliable plasma modeling and process optimization. The complexity of plasma–surface interactions—arising from incident particle bombardment, surface roughness, contamination, and continuous surface modification due to etching or deposition—makes it challenging to assign accurate and reproducible values to these surface coefficients. Moreover, most γ values reported in the literature for individual species have been obtained from beam experiments carried out in ultrahigh-vacuum setups employing cleaned and well characterized surfaces [11, 33–35]. Although such experiments provide essential reference data and are widely used in plasma simulations, their direct relevance to practical discharge systems remains limited. Under realistic conditions, electrode surfaces undergo continuous modification due to plasma exposure, which introduces uncertainties that can compromise both the accuracy and the predictive capacity of numerical models, particularly in studies targeting accurate control of discharge dynamics and plasma–surface interactions.

To overcome the challenges associated with determining γ, numerous experimental and computational approaches have been developed over the past decade. Typically, these investigations integrate plasma diagnostics—such as optical emission spectroscopy, electron density measurements, and ion energy analysis—with kinetic simulations, allowing the extraction of surface parameters by matching experimental data with numerical predictions. For instance, Daksha *et al* [36] introduced the γ—CAST method, where spatio-temporal excitation profiles in argon capacitive discharges were analyzed to correlate variations in excitation dynamics with the effective γ. Schulenberg *et al* [37] combined Langmuir-probe measurements and ion flux–energy spectra, obtained using a retarding-field energy analyzer, to determine both γ and the electron reflection coefficient, R. Subsequently, Schulze *et al* [38] employed high-resolution energy-resolved ion mass spectrometry to examine the bimodal peak shape of the ion flux–energy distribution, enabling the evaluation of γ and R for stainless steel and aluminum oxide electrodes. The material dependence of effective SEE yields under plasma conditions has also been investigated in a geometrically symmetric CCP operated in argon with a 10% neon admixture [39]. In that study, excitation dynamics and power absorption were analyzed for different electrode materials (e.g. copper, nickel, gold, aluminum, and stainless steel) across a range of voltages and pressures. The effective γ values were determined *in-situ* by combining phase-resolved optical emission spectroscopy measurements with particle-in-cell/Monte Carlo collision (PIC/MCC) simulations, demonstrating that secondary emission can vary significantly with electrode material and highlighting the importance of accounting for realistic surface conditions in plasma modeling.

In our recent study [40], the effective secondary electron emission coefficient, γ, was determined *in-situ* for argon capacitive RF discharges with stainless-steel electrodes. By comparing experimentally obtained DC self-bias voltages with results from simulations, the effective γ was found to vary between approximately 0.058 and 0.081 across the examined discharge conditions (with an estimated uncertainty of ± 0.01). (For a discussion of the uncertainty see [40].) These values are consistent with those reported in the literature for argon plasmas. The approach itself was originally proposed in our earlier work

[41], where we have found that the DC self-bias voltage (η) is sensitive to changes in γ under temporally asymmetric excitation, a condition that gives rise to the electrical asymmetry effect (EAE) [42–45].

Based on these results, the present work extends the previously developed methodology to CCPs operated in neon and helium. Helium ions, in particular, are known for their large potential energy and strong tendency to induce secondary electron emission, while neon shows intermediate behavior between helium and argon in terms of both ionization dynamics and electron emission efficiency. By applying our previously validated approach to these gases, we aim to provide a comprehensive assessment of SEEC behavior across different noble gases. To ensure a direct comparison with our previous study, we maintain similar experimental and numerical setups, adjusting only the necessary parameters to account for the different physical properties of neon and helium. This approach allows us to systematically analyze the impact of gases on the measured self-bias voltage and extract reliable SEEC values for these gases. The paper is structured as follows: section 2 provides the experimental and numerical methods applied in this work. Section 3 discusses the main results, and section 4 offers a conclusion to this study.

2. Methods

2.1. Experimental setup

In our previous study on argon discharges [40], we presented an *in-situ* method for determining the effective SEEC, γ, using the EAE. This effect is typically achieved in geometrically symmetric capacitive discharges by applying a multi-frequency voltage waveform [42]:

$$\phi_0(t) = \sum_{k=1}^{N_H} \phi_k \cos(k2\pi f_1 t + \theta_k), \tag{1}$$

where N_H denotes the number of harmonics, f_1 is the base frequency, ϕ_k and θ_k denote the amplitude and phase associated with the kth harmonic, respectively. As a result of the EAE-induced asymmetry, a DC self-bias voltage, η, is established, and the voltage across the plasma can be expressed as

$$\phi(t) = \phi_0(t) + \eta. \tag{2}$$

The same excitation principle is adopted in the present work, and is realized in a symmetrically configured CCP reactor. Analysis of our previous results [40, 41], showed that accurate *in-situ* determination of γ, via the EAE requires CCP systems that (i) enable precise RF voltage measurements and (ii) exhibit a strong sensitivity of the DC self-bias voltage to variations in SEE yield, γ. To meet these requirements, we have identified an appropriate set of excitation parameters—fundamental driving frequency (f_1), number of harmonics (N_H), voltage amplitudes (ϕ_k), and gas pressure (p)—for argon discharges. Extending this approach to helium and neon, we selected similar parameter ranges, accounting for the distinct plasma properties of these gases. The experiments are operated in our 'XS Cell,' which is a simple symmetric CCP cell with electrodes (stainless steel) of 92 mm diameter, separated by a 27.5 mm gap between them. The details of this setup and its advantages are described in detail in [40]. Here, we briefly summarize its key aspects relevant to the present study. To achieve a balance between maximizing the DC self-bias voltage and minimizing technical difficulties in waveform generation, the harmonics number of the applied waveform, N_H, is set to 2 based on previous findings [40]. The applied waveform is expressed as:

$$\phi_0(t) = \phi_1 \cos(2\pi f_1 t) + \phi_2 \cos(4\pi f_1 t + \theta), \tag{3}$$

with the fundamental frequency of $f_1 = 4$ MHz. Equation (3) defines the RF voltage waveform supplied by the generator, while the DC self-bias voltage η develops self-consistently due to the EAE and is added as a time-independent offset to obtain the total electrode potential $\phi(t)$ (see equation(2)).

This relatively low frequency enhances the accuracy of RF voltage measurements and the selected pressures and voltage amplitudes are chosen to ensure a pronounced influence of secondary electron emission on the discharge characteristics while maintaining stable plasma conditions. Specifically, for helium, pressures of 120 Pa and 240 Pa are selected with voltage amplitudes of $\phi_1 = 160$ V and $\phi_2 = 80$ V, for neon, gas pressures of 80 Pa and 160 Pa are used, keeping the same voltage amplitudes as for helium. (The $\phi_1/\phi_2 = 2$ ratio is known to maximize the DC self bias for a given ϕ_1 [46].)

To implement the waveform in equation (3) in the experiment, a dedicated setup is employed to generate and precisely control the excitation signal applied to the powered electrode. A RF signal generator with two channels (Multicomp Pro MP750389) provides independent control of the amplitudes and phase angles of the fundamental and second-harmonic components. Its output is amplified by a RF amplifier (Vectawave VBA100-200) and delivered to the powered electrode through a low-pass filter (custom built 5th order Chebyshev type with 8.1 MHz cutoff frequency) to suppress unwanted higher harmonics. The RF voltage is monitored using an oscilloscope (Tektronix MSO44) with a high-voltage probe (P5100A). The generator parameters were adjusted by a computer running a LabVIEW-based feedback loop linked to the oscilloscope to match the desired waveform at the electrode. As minor deviations between the measured and theoretical waveforms remain, the experimentally recorded waveforms are used as simulation input, following the approach in our previous work [40]. Examples of the corresponding voltage waveforms at different θ values are provided in [40], offering additional insight into the phase-dependent waveform characteristics.

2.2. Computational method

Numerical studies are based on a one-dimensional in space and three-dimensional in velocity space (1d3v) electrostatic PIC/MCC code [47–50]. The simulation code has been benchmarked against experimental data for CCPs, demonstrating good agreement with spatially and temporally resolved optical emission measurements in neon discharges [51]. The model considers singly charged ions and electrons, and includes a set of elementary collision processes. For both helium and neon discharges, electron–neutral collisions include elastic scattering, excitation, and ionization, with the corresponding cross sections adopted from the Biagi-v8.9 dataset [52], available via the LxCat database [53]. Ion–neutral collisions (He^+–He and Ne^+–Ne) are also included, with cross section data taken from [54]. For both gases, isotropic and backward scattering channels are considered.

In the simulations, the electrode at $x = 0$ is driven by an experimentally recorded voltage waveform to enable direct comparison, while the electrode, located at $x = L$ is grounded. The electrostatic approximation [55] is adopted in the simulations. To provide sufficient spatial resolution (Δx) for the electric potential and particle density calculations, equidistant grids with $N_g = 500$ and $N_g = 800$ points are used for helium and neon, respectively. The number of time steps per RF period, N_t, is chosen according to the base driving frequency and the gas pressure so that the collision probability within one step remains below 5%. For helium, $N_t = 31\,200$ and $62\,000$ are used at 120 and 240 Pa, respectively, while for neon, $N_t = 24\,000$ and $48\,000$ correspond to 80 and 160 Pa. The electric potential is obtained by solving the Poisson equation via the Thomas algorithm. The boundary conditions are defined by the electrode potentials, while the space charge is obtained from the distribution of the particles. The leapfrog scheme is used for integrating the equation of charged particles motion. Electrons are advanced at every time step (Δt_e) while He^+ ions are advanced every 10th time step ('ion subcycling') and Ne^+ ions are advanced in each 20th time step ($\Delta t_i = 10\Delta t_e$ for He^+, $\Delta t_i = 20\Delta t_e$ for Ne^+). The chosen numerical parameters fulfill the stability and accuracy requirements of electrostatic PIC/MCC simulations (see, e.g. [55–58]).

In the simulations, the interaction between plasma particles and the electrode surfaces accounts for (i) elastic reflection of incident electrons, characterized by reflection coefficient, R, and (ii) ion-induced secondary electron emission, characterized by SEE yield, γ. Although a more realistic treatment of electron reflection at electrode surfaces would consider the dependence of the reflection coefficient on the electron energy [59], angle of incidence, and surface properties [28], a simplified approach using a constant reflection probability (appropriate at the conditions covered) is adopted in this study. Accordingly, we assume a fixed value of $R = 0.7$ following the earlier study [38]. To extract the ion-induced SE yield, γ, simulations are performed using a set of different γ values while keeping all other discharge parameters unchanged. The value consistent with the experiment is identified by comparing the computed DC self-bias voltage with the experimentally measured one.

In this work, the secondary electron emission coefficient γ is treated as an effective parameter. The value of γ obtained from the comparison between experimental measurements and PIC/MCC simulations represents an effective secondary electron emission coefficient, which implicitly includes contributions from additional emission mechanisms, such as metastable- or photon-induced processes.

The DC self-bias voltage, η, is adjusted in the simulations through an iterative procedure. At the beginning, η is set to zero, and the discharge is simulated for several RF periods. The average electron and ion currents to the electrodes are then compared. If a difference between these currents is found, η

is slightly modified and the simulation is continued. This cycle continues until the time-averaged electron and ion currents become equal at both electrodes. Accordingly, η represents the time-averaged DC potential of the powered electrode with respect to the grounded electrode. The simulations are run for thousands of RF cycles until the number of superparticles and DC self-bias voltage reach a steady state. Once convergence is achieved, diagnostics data are collected over an additional 100 RF periods.

It has to be kept in mind that the one-dimensional computational approach cannot account for the effect of losses due to radial particle transport in the experimental system. With the dimensions of the discharge cell, these fluxes are not expected to be significant as compared to the fluxes to the electrodes which are driven by the much stronger axial electric field as compared to the radial ambipolar field. Nonetheless, we admit that extending the simulation to two dimensions could provide more accurate results, but this extension remains as future work.

3. Results

Experiments and PIC/MCC simulations are performed under the following conditions: for helium, the discharge operates at 120 Pa and 240 Pa, while for neon the pressures are 80 Pa and 160 Pa. The other parameters are identical in all cases, with the fundamental frequency fixed at 4 MHz and the amplitudes of the two voltage harmonics set to $\phi_1 = 160$ V and $\phi_2 = 80$ V. The electrodes are separated by a gap of $L = 2.75$ cm. The effective secondary electron emission coefficient γ is varied from 0 to 0.3 for helium and from 0 to 0.2 for neon in the PIC/MCC simulations.

Figure 1 shows the experimentally determined DC self-bias voltage η as a function of the phase angle θ for helium and neon at different pressures (solid curves). Panels (a) and (b) present the measurements for helium at 120 Pa and 240 Pa, respectively, while panels (c) and (d) display the corresponding results for neon at 80 Pa and 160 Pa. The symbols indicate the computed values of the DC self-bias obtained under the same discharge conditions as in the experiment for the phase angle of $\theta = 350°$. This phase is selected because the measured $\eta(\theta)$ curve is relatively flat in this region, minimizing the impact of small phase uncertainty due to the experimental signal delay.

As can be seen, the form of the $\eta(\theta)$ curve shows good consistency with earlier experiments and simulations results [40]. Depending on the discharge conditions, the extrema of the DC self-bias reach values of $|\eta| \approx 35$–50 V. A small angular displacement of these extrema is also observed. This shift, which originates from the charge dynamics inside the sheaths, has been discussed for argon discharges and appears here as well in helium and neon (see [40] for details). The comparison of the computational and experimental results reveals two clear trends: (i) the DC self-bias decreases as the effective secondary electron emission coefficient γ increases, in line with our earlier findings [40, 41], and (ii) under the present conditions the effective SEE falls within $0 \leqslant \gamma \leqslant 0.2$ for both gases. The corresponding values for each case are summarized in table 1.

Figure 2 illustrates the response of the DC self-bias voltage to changes in γ for (a) helium (120 Pa and 240 Pa) and (b) neon (80 Pa and 160 Pa). The symbols represent the PIC/MCC simulation results, while the solid curves correspond to parabolic fits to these data. The horizontal dashed lines indicate the experimentally measured DC self-bias voltages. The effective values of γ are obtained from the intersections between the fitted curves and the experimental values presented by thin vertical gray lines. The resulting values are listed in table 2.

For the stainless steel electrodes, for helium, we obtain $\gamma = 0.105$ at 120 Pa and $\gamma = 0.165$ at 240 Pa. For neon, the values are $\gamma = 0.074$ at 80 Pa and $\gamma = 0.104$ at 160 Pa. These values are considerably lower than the constant secondary-electron yields that are often assumed in simplified CCP models, in which fixed γ values are used primarily as tuning parameters to match selected experimental parameters through PIC/MCC simulations. A different approach was taken by Daksha *et al* [60], who developed an *ab initio* approach based on Hagstrum's theory of Auger emission, enabling predictions of γ for various ion species and clean metal surfaces. Their model accounts for material- and energy-dependence, and simulations demonstrate that simplified or constant γ values can lead to substantial discrepancies in CCP behavior. For validation, Daksha *et al* compared their model predictions with a broad range of experimental data reported in the literature [33, 61–67]. Moreover, Pamperin *et al* [68] applied a quantum-kinetic (Anderson–Newns) model to compute emission spectra and secondary electron yields for He^+ impact on metallic surfaces and benchmarked their predictions against the experimental data of Müller *et al* [69]. for W(110) Müller *et al* [69] performed direct measurements of γ for rare gas ions, including He^+ and Ne^+, W(110) and cesiated W(110) and Au surfaces. Table 3 summarizes representative γ values for He^+ and Ne^+ from the literature, both experimental and theoretical. Our results for both gases fall within the experimental range of data.

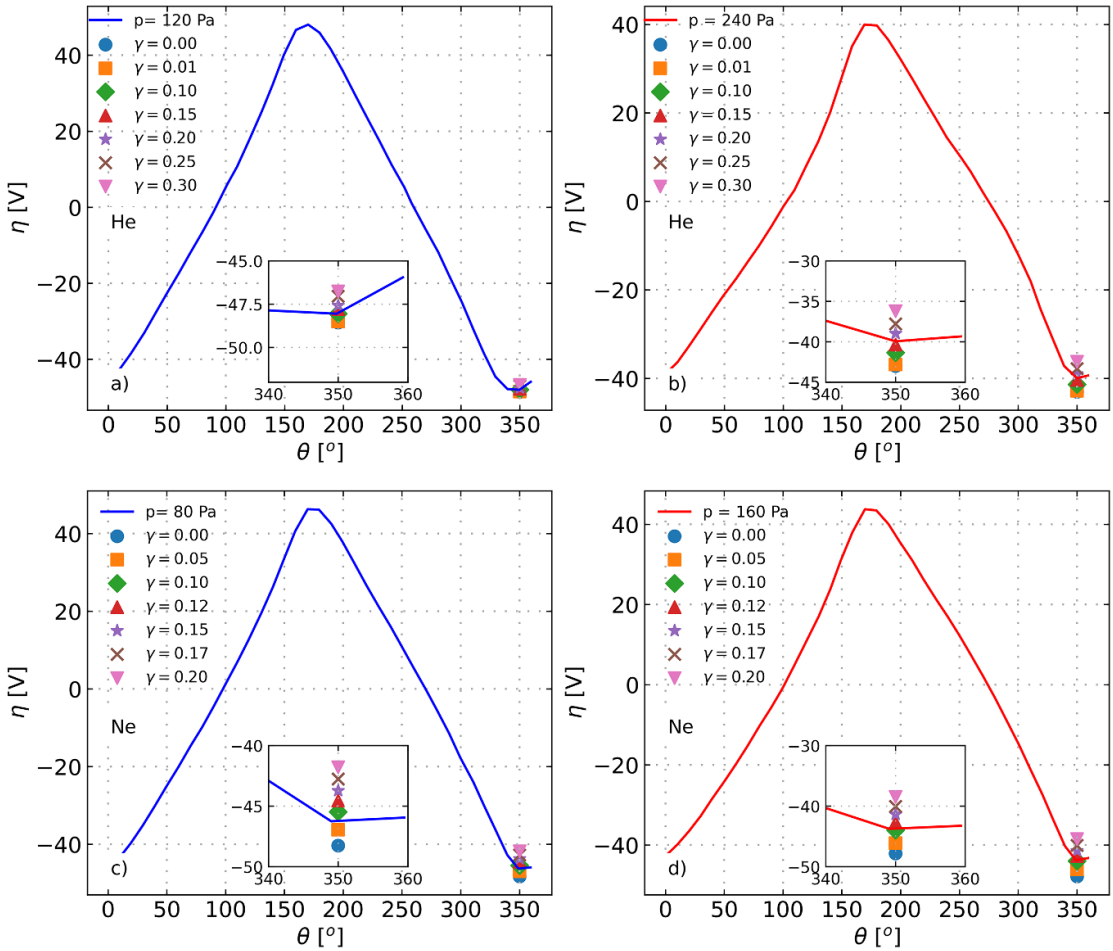


Figure 1. Dependence of the experimentally obtained DC self-bias voltage η on the phase angle θ for helium and neon discharges at different pressures. The top panels show results for helium at 120 Pa (a) and 240 Pa (b), while the bottom panels correspond to neon at 80 Pa (c) and 160 Pa (d). Symbols represent the DC self-bias voltages obtained from the simulations at $\theta = 350°$ for helium and neon, with γ values ranging from 0 to 0.3 and from 0 to 0.2, respectively.

Table 1. Computed extrema of the DC self-bias voltage η as a function of the effective SEEC γ for the various discharge conditions in He and Ne.

Helium (He)				Neon (Ne)			
120 Pa		240 Pa		80 Pa		160 Pa	
γ	η (V)	γ	η (V)	γ	η (V)	γ	η (V)
0.0	−48.6	0.0	−43.0	0.0	−48.3	0.0	−47.8
0.01	−48.5	0.01	−42.8	0.05	−46.9	0.05	−46.1
0.1	−48.1	0.1	−41.4	0.1	−45.5	0.1	−43.9
0.15	−47.8	0.15	−40.4	0.125	−44.5	0.125	−42.7
0.2	−47.6	0.2	−38.9	0.15	−43.7	0.15	−41.4
0.25	−47.0	0.25	−37.8	0.175	−42.8	0.175	−40.1
0.3	−46.8	0.3	−36.2	0.2	−41.8	0.2	−38.5

Figure 3 presents a comparison between the experimentally measured and numerically obtained DC self-bias voltage as a function of the phase angle θ for two different gases. Panel (a) corresponds to helium at $p = 120$ Pa with $\gamma = 0.105$, while panel (b) shows neon at $p = 80$ Pa with $\gamma = 0.074$. For both gases, the $\eta(\theta)$ dependencies derived from simulations fully reproduce the experimental results for the whole range of the phase angle. This confirms the consistency of the model and supports the corresponding effective secondary electron emission coefficient used for these conditions.

Following the methodology of our previous investigations [40, 41], the analytical description of the EAE [42, 71] is applied here to interpret how the DC self-bias voltage depends on the secondary electron

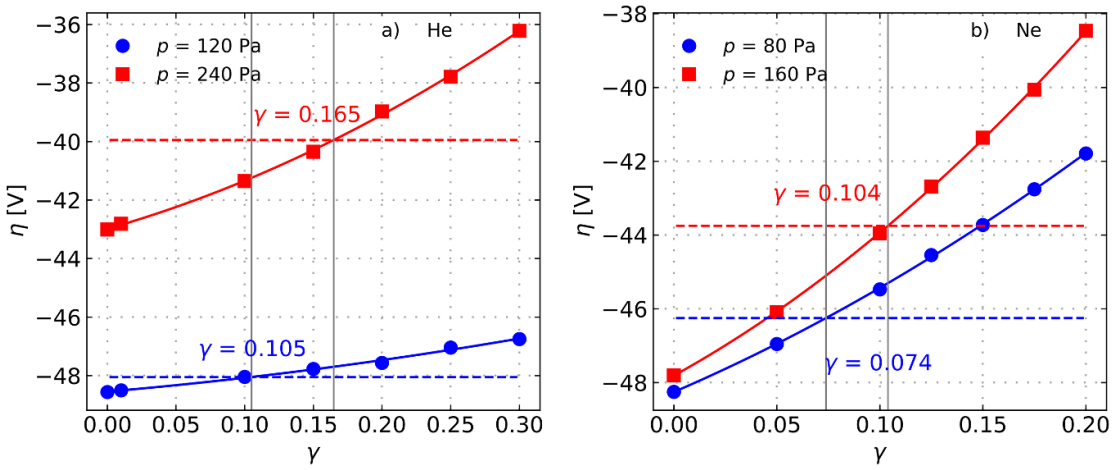


Figure 2. Dependence of the computed DC self-bias voltage, η, at $\theta = 350°$ on γ for (a) helium ($p = 120$ Pa and 240 Pa) and (b) neon ($p = 80$ Pa and 160 Pa). Discharge conditions: $f_1 = 4$ MHz, $\phi_1 = 160$ V, $\phi_2 = 80$ V, and $L = 2.75$ cm. The symbols represent the simulation results, while the solid curves show their parabolic fits. Horizontal dashed lines indicate the experimentally measured DC self-bias voltages.

Table 2. Experimentally measured values of the DC self-bias voltage η and the effective secondary electron yield γ for the different conditions of the discharge.

Gas	p	η	γ
He	120 Pa	−48.05 V	0.105
He	240 Pa	−39.95 V	0.165
Ne	80 Pa	−46.25 V	0.074
Ne	160 Pa	−43.75 V	0.104

emission coefficient. Within this framework, the DC self-bias voltage, η, can be expressed as

$$\eta = \overbrace{-\frac{\phi_{\max} + \varepsilon\phi_{\min}}{1+\varepsilon}}^{\text{Term 1}} + \overbrace{\frac{\phi^{\mathrm{f}}_{\mathrm{sp}} + \varepsilon\phi^{\mathrm{f}}_{\mathrm{sg}}}{1+\varepsilon}}^{\text{Term 2}} + \overbrace{\frac{\phi^{\mathrm{b}}_{\max} + \varepsilon\phi^{\mathrm{b}}_{\min}}{1+\varepsilon}}^{\text{Term 3}}, \tag{4}$$

where, $\phi_{\max}$ and $\phi_{\min}$ denote the extrema of the applied voltage. The quantity $\phi^{\mathrm{f}}_{\mathrm{sp}}$ corresponds to the floating potential at the powered electrode, while $\phi^{\mathrm{f}}_{\mathrm{sg}}$ refers to that at the grounded electrode. The terms $\phi^{\mathrm{b}}_{\max}$ and $\phi^{\mathrm{b}}_{\min}$ describe the instantaneous potential drop across the plasma bulk at the moments of maximum and minimum applied voltage. The symmetry parameter, ε, is the ratio of the peak values of the sheath voltages at both sides of the plasma

$$\varepsilon = \left|\frac{\widehat{\phi}_{\mathrm{sg}}}{\widehat{\phi}_{\mathrm{sp}}}\right| = \left(\frac{A_{\mathrm{p}}}{A_{\mathrm{g}}}\right)^2 \frac{\overline{n}_{\mathrm{sp}}}{\overline{n}_{\mathrm{sg}}} \left(\frac{Q_{\mathrm{mg}}}{Q_{\mathrm{mp}}}\right)^2 \frac{I_{\mathrm{sg}}}{I_{\mathrm{sp}}} \approx \frac{\overline{n}_{\mathrm{sp}}}{\overline{n}_{\mathrm{sg}}} \left(\frac{Q_{\mathrm{mg}}}{Q_{\mathrm{mp}}}\right)^2, \tag{5}$$

here $|\widehat{\phi}_{\mathrm{sp}}|$ and $|\widehat{\phi}_{\mathrm{sg}}|$ are the maximum voltage drops across the sheaths at the powered and grounded electrode. The quantities $Q_{\mathrm{mp/mg}}$ represent the peak uncompensated charges in the respective sheaths, while $A_{\mathrm{p/g}}$ correspond to the electrode surface areas. The terms $I_{\mathrm{sp/sg}}$ refer to the sheath integrals, and $\overline{n}_{\mathrm{sp/sg}}$ to the mean charge densities. Following [42, 71], the ratio of sheath integrals is taken as unity, and the electrode areas are identical ($A_{\mathrm{p}} = A_{\mathrm{g}}$) due to the symmetric configuration. All the remaining input parameters of the model are taken from the PIC/MCC simulation, while the sheath widths are defined according to the Brinkmann sheath criterium [42, 72].

The DC self-bias obtained from the analytical model, along with the individual contributions of the three terms in equation (4) and the symmetry parameter ε, are shown in figure 4 for both helium (top row) and neon (bottom row). Panels (a, d) compare the DC self-bias from PIC simulations (marked as 'PIC') with model predictions (marked as 'Model'), where simulation-derived values are used for all input parameters in equation (4). The panels also include 'Term 1', representing the contribution from the asymmetry of the applied voltage waveform. A good agreement is found between the model and

Table 3. Comparison of experimentally measured and calculated effective secondary-electron emission coefficients, γ, for He^+/Ne^+ impact on metallic surfaces (compiled from literature).

Surface materials	Experimental γ	Theory γ
He^+		
Ni (111)	0.170 [61]	0.177 [60]
C contaminated Mo	0.247 [62]	0.275 ± 0.005 [60]
He contaminated Ta	0.14 [63]	0.13 [60]
Au	0.16 [66], 0.18 ± 0.02 [67]	0.26 [60]
Mo	0.286 [62], 0.300 [33], 0.20 [64]	0.287 [60]
Pt	—	∼0.18 [60]
Cu	—	∼0.28 [60]
Ca	—	∼0.3 [60]
Al	—	∼0.09 [68]
Cu	—	∼0.10 [68]
W(110)	0.22 [69]	∼0.12 [68]
Au	0.16 [69]	—
Cs/W(110)	0.28 [69]	—
Stainless steel	0.105–0.165 [present work]	—
Ne^+		
Ni (111)	0.128 [61]	0.111 [60]
K	0.38 ± 0.01 [65]	0.23 ± 0.01 [60]
Na	0.36 ± 0.01 [65]	0.27 ± 0.01 [60]
Ba	0.34 ± 0.01 [65]	0.28 ± 0.01 [60]
Zr	0.14 [65]	0.22 [60]
Ni	0.19 ± 0.01 [65]	0.19 [60]
Au	0.15 ± 0.02 [67]	0.21 [60]
Mo	0.254 [33], 0.228 [70]	0.247 [60]
Ta	0.23 ± 0.01 [65]	0.11 ± 0.01 [60]
Pt	0.07 ± 0.01 [65]	0.08 [60]
W(110)	0.16 [69]	—
Au	0.13 [69]	—
Cs/W(110)	0.17 [69]	—
Stainless steel	0.074–0.104 [present work]	—

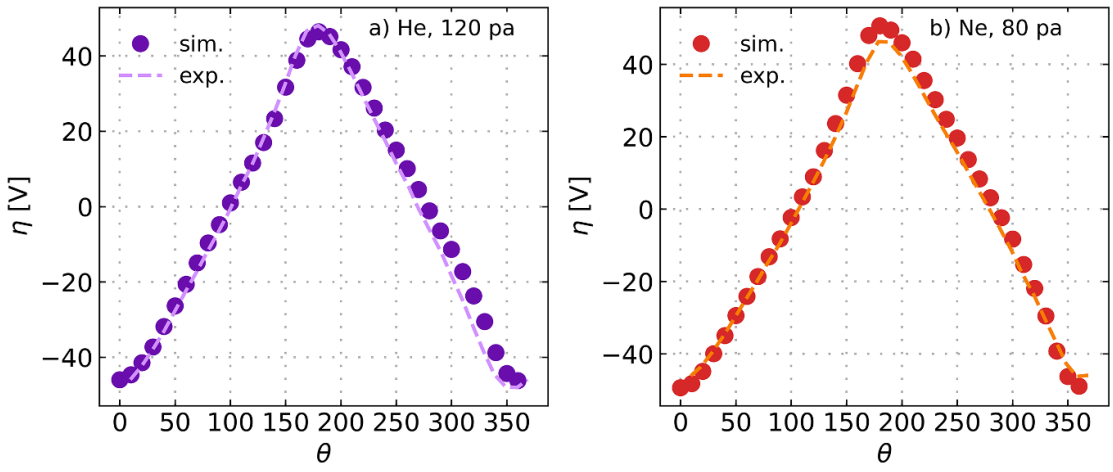


Figure 3. Measured and computed DC self-bias voltage η as a function of the phase angle θ: (a) helium at $p = 120$ Pa, $\gamma = 0.105$; (b) neon at $p = 80$ Pa, $\gamma = 0.074$. The discharge parameters are: $f_1 = 4$ MHz, $\phi_1 = 160$ V, $\phi_2 = 80$ V, and $L = 2.75$ cm. The symbols denote simulation results, the dashed lines represent experimental data.

the simulation results. In both gases, 'Term 1' dominates the total DC self-bias. Panels (b, e) illustrate the contributions of the second and third terms in equation (4), representing the effects of the floating sheath potentials and the plasma bulk voltage drop, respectively. These terms are significantly smaller than 'Term 1' in both gases but contribute more in helium—together accounting for ≈9%–10% of the total bias—than in neon (≈3%–4%). The second term remains nearly constant, while the third term decreases slightly in helium and increases with γ in neon. The opposite functional dependence 'Term 3'

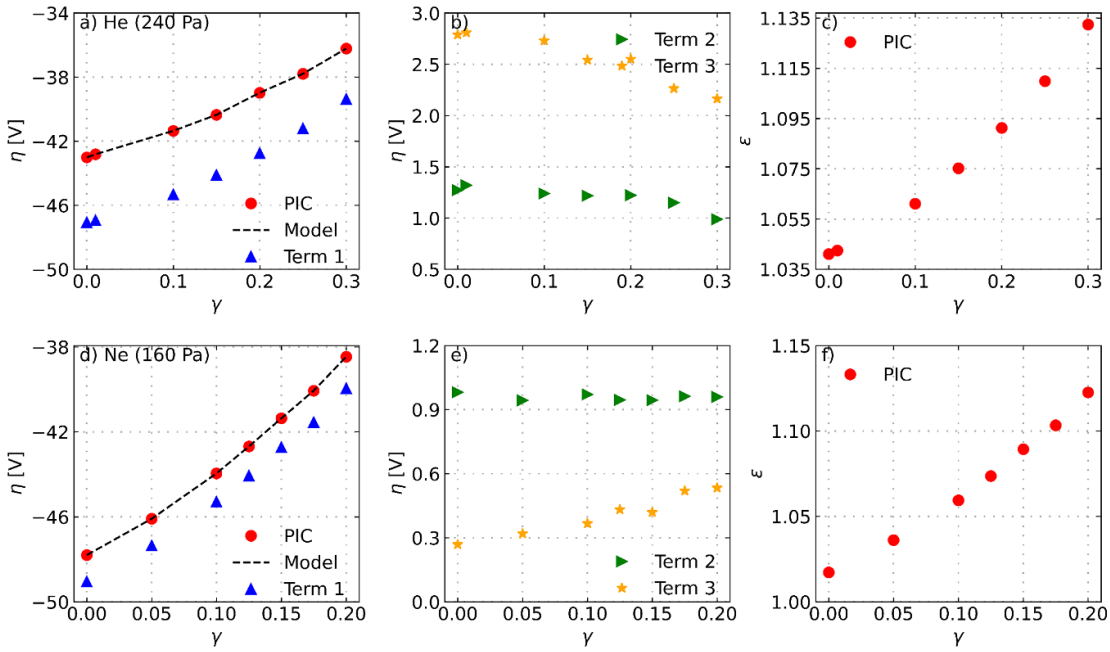


Figure 4. DC self-bias voltage, η, (a, b, d, e) and symmetry parameter, ε, (c, f) as functions of the secondary electron emission coefficient, γ, obtained from PIC/MCC simulations and the EAE analytical model at $\theta = 350°$. Discharge conditions: He at 240 Pa (top row), Ne at 160 Pa (bottom row): $f_1 = 4$ MHz, $L = 2.75$ cm, $R = 0.7$. In panels (a, d), PIC/MCC results are compared to the full model (dashed line) and Term 1 only (blue triangles), which accounts for the effect of the applied voltage waveform asymmetry on the DC self-bias voltage. Panels (b, e) show contributions from Terms 2 and 3 of the model, corresponding to the effects of floating potentials and bulk voltage drops, respectively, as described by equation (4). Panels (c) and (f) present the symmetry parameter ε obtained from PIC/MCC simulations.

vs. γ as well as the opposite relative importance of 'Term 2' vs 'Term 3' in He and Ne originates from the complex charged particle dynamics and the different phase shifts between the discharge voltage and current as a function of the gas and the operating conditions. These effects do not influence the findings of the present study, and will be a subject of further investigations.

We also examine how the symmetry parameter varies with the secondary electron emission coefficient, as shown in panels (c, f) of figure 4. Since the DC self-bias η is sensitive to variations in γ, its change can be primarily attributed to the behavior of ε. In equation (4), the quantities $\phi_{\max}$ and $\phi_{\min}$ remain constant for a given phase angle, implying that the γ-dependence of the η entirely arises from the variation of the symmetry parameter. The data show that ε increases monotonically with γ, which reflects the underlying change of the peak sheath voltages as the secondary electron emission coefficient increases (see equation (5)). Understanding the dependence of the DC self-bias voltage on γ requires analyzing the response to changes in γ of two key ratios: the maximum uncompensated charges in the grounded and powered sheaths, $Q_{\mathrm{mg}}/Q_{\mathrm{mp}}$, and the ratio of the mean charged particle densities, $\overline{n}_{\mathrm{sp}}/\overline{n}_{\mathrm{sg}}$.

Figure 5 shows (a, d) the time-averaged spatial density distributions of electrons and ions across the electrode gap, n, (b, e) the corresponding time-averaged ionization rate profiles, $S(x)$, and (c, f) the temporal evolution of the total uncompensated charge per unit area, Q/A, during one RF period for a sequence of γ values. The top row corresponds to helium (at $p = 240$ Pa), while the bottom row presents the analogous results for neon (at $p = 160$ Pa). For all density plots, the electron density is shown with solid lines and the ion density (He^+, Ne^+) with dashed lines. The color of each curve corresponds to a specific value of γ, as indicated in the legends above the panels. Additionally, key parameters—such as the ratio $\overline{n}_{\mathrm{sp}}/\overline{n}_{\mathrm{sg}}$, the charge ratio $Q_{\mathrm{mg}}/Q_{\mathrm{mp}}$, and the peak sheath voltages—are presented in figure 6. Complete datasets for different γ values at $\theta = 350°$ are summarized in tables 4–7 in the appendix.

With increasing values of the SEEC, γ, plasma density increases in both gases and becomes more asymmetric with respect to the discharge center, which is directly linked to the overall enhancement of the time-averaged ionization rate, $S(x)$, shown in panels (b, e) for both gases. This increase is more pronounced near the powered electrode, where the sheath is expanded for a longer time during the RF period compared to the grounded electrode because of the applied voltage waveform. Consequently, secondary electrons emitted from the powered electrode have more time to gain energy within the

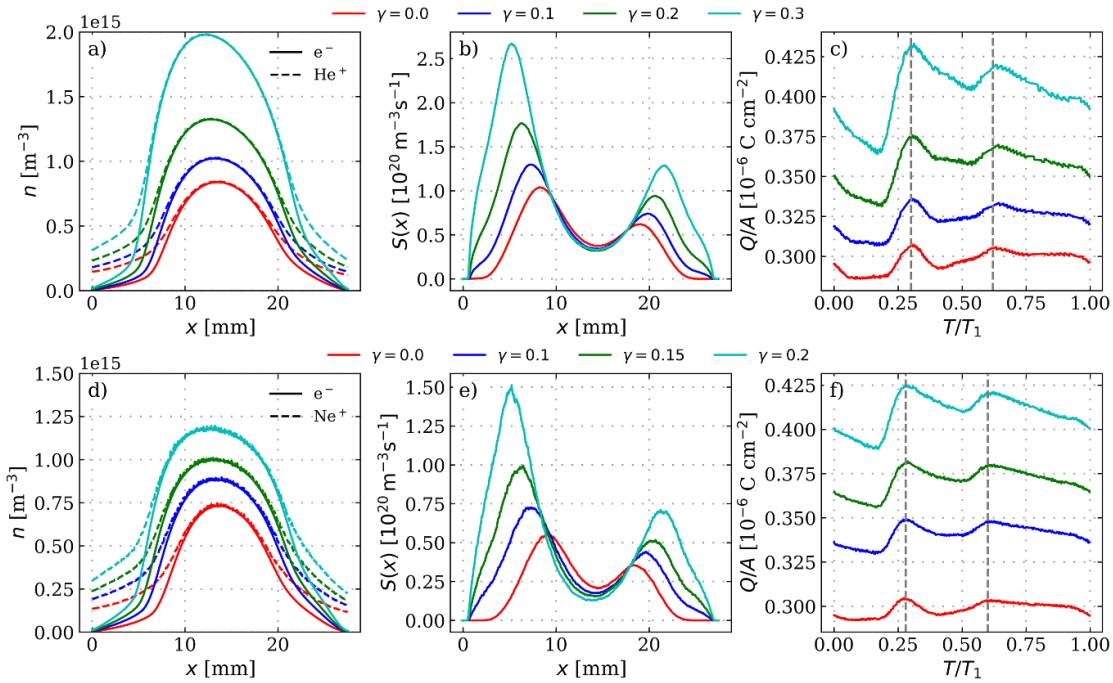


Figure 5. Spatial profiles of the time-averaged electron and ion densities, n, (a, d), ionization rate $S(x)$ (b, e), and temporal evolution of the total uncompensated charge per unit area during one RF cycle (c, f) for different values of the secondary electron emission yield γ. The top row corresponds to helium ($p = 240$ Pa) and the bottom row to neon ($p = 160$ Pa). The vertical dashed lines in (c, f) mark the times of sheath collapse: $t_p/T_1 \approx 0.3$ (powered electrode) and $t_g/T_1 \approx 0.6$ (grounded electrode). In the density plots (a, d), electron densities are shown with solid lines, while ion densities (He^+, Ne^+) are shown with dashed lines. Different colors correspond to different values of γ. Discharge conditions: $L = 2.75$ cm, $f_1 = 4$ MHz, $\phi_1 = 160$ V, $\phi_2 = 80$ V, $R = 0.7$, $\theta = 350°$.

sheath, which increases their contribution to ionization. This mechanism explains the observed increase of the ratio $\overline{n}_{sp}/\overline{n}_{sg}$ with increasing γ, as shown in figure 6 and in tables 4–7.

To understand the behavior of the $(Q_{mg}/Q_{mp})^2$ term contributing to ε (see equation (5)), one can examine how the total uncompensated plasma charge, Q, varies with the secondary electron emission coefficient, γ. Figures 5(c, f) shows the temporal evolution of this charge, normalized to the electrode area A, during one fundamental RF period, as determined by the alternating electron and ion currents at the electrodes. The increase in Q/A occurs as electrons are removed from the plasma, while its subsequent decrease results from the continuous ion loss to the electrodes. The moments corresponding to sheath collapses in panels (c, f) are indicated by vertical dashed lines. The first event, occurring at $t_p/T_1 \approx 0.3$, represents the collapse of the sheath at the powered electrode, whereas the second, at $t_g/T_1 \approx 0.6$, corresponds to the collapse at the grounded side. Accordingly, at $t = t_p$, the data display Q_{mg}/A, while at $t = t_g$, the data show Q_{mp}/A, as the charge maxima in one sheath coincide with the collapse of the opposite sheath. The results in figure 5(c) demonstrate a clear monotonic growth of the ratio Q_{mg}/Q_{mp} with increasing γ, as shown in tables 4 and 5. This result of the enhanced ionization near the powered electrode, producing on average a higher positive ion flux toward this electrode than toward the grounded one. To maintain the balance between the time-averaged positive and negative particle fluxes, a correspondingly higher electron current is required at the powered side. Consequently, during the sheath collapse at the powered electrode, the quantity Q/A exhibits a more pronounced increase than during the collapse at the grounded side.

To further illustrate the electrostatic potential structure, spatial profiles of the time-averaged potential $\langle\phi(x)\rangle_t$ are shown in figure 7 for different values of γ. The experimentally measured DC self-bias voltage η is indicated by a horizontal dashed line.

In helium (figure 6(b)), both $\overline{n}_{sp}/\overline{n}_{sg}$ and $(Q_{mg}/Q_{mp})^2$ increase with γ, which raises the symmetry parameter ε and thus reduces $|\eta|$. In neon (figure 6(d)), $\overline{n}_{sp}/\overline{n}_{sg}$ increases whereas $(Q_{mg}/Q_{mp})^2$ remains nearly constant (variation $\lesssim 2\%$) with γ. Hence, the change in ε is dominated by the density-ratio factor, in agreement with the observed trend of the DC self-bias.

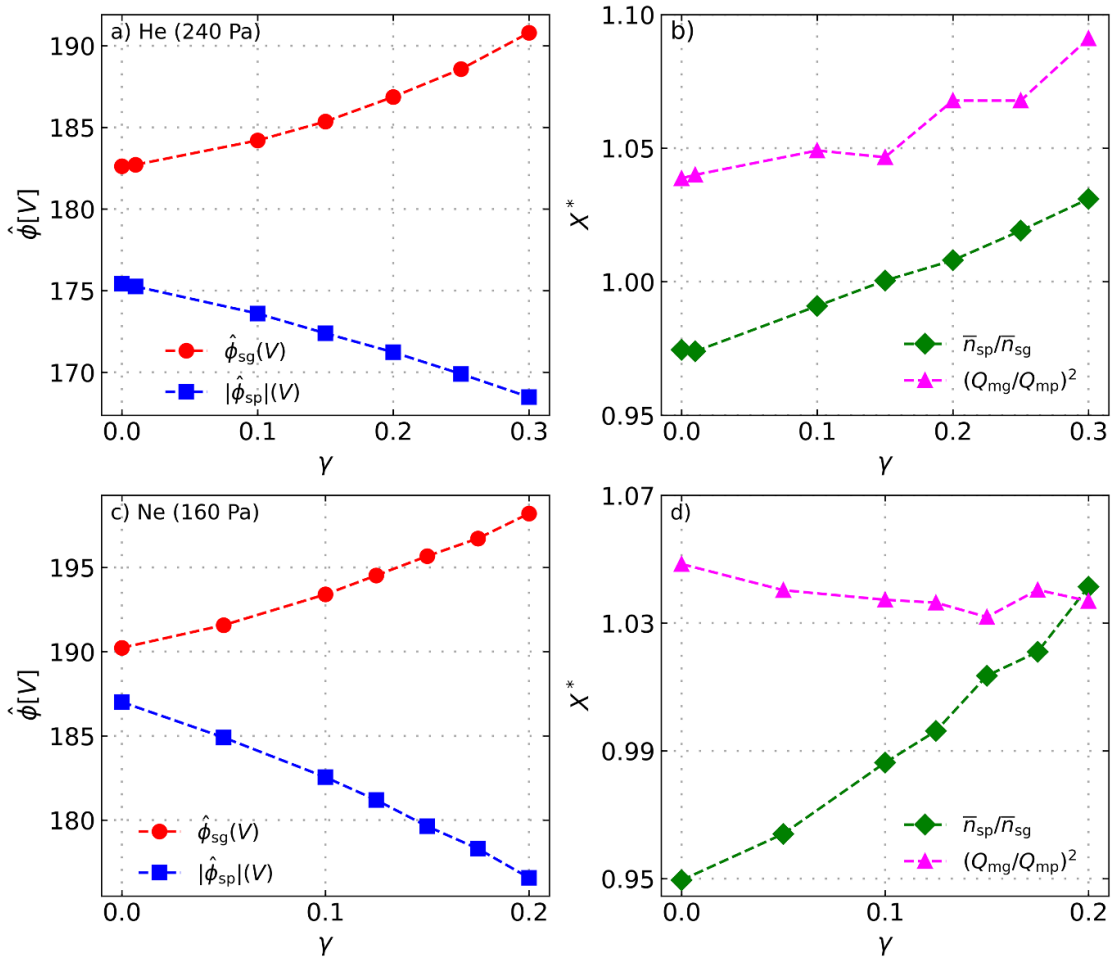


Figure 6. Peak sheath voltage values at the powered ($|\widehat{\phi}_{sp}|$) and grounded ($\widehat{\phi}_{sg}$) electrodes (a, c) and the ratios (X^*) of the mean charged particle densities in the respective sheaths, $\overline{n}_{sp}/\overline{n}_{sg}$, and the maximum uncompensated sheath charges, $(Q_{mg}/Q_{mp})^2$, as functions of γ (b, d) for He (top row: $p = 240$ Pa) and Ne (bottom row: $p = 160$ Pa). Discharge conditions: $L = 2.75$ cm, $f_1 = 4$ MHz, $\phi_1 = 160$ V, $\phi_2 = 80$ V, $R = 0.7$, at $\theta = 350°$.

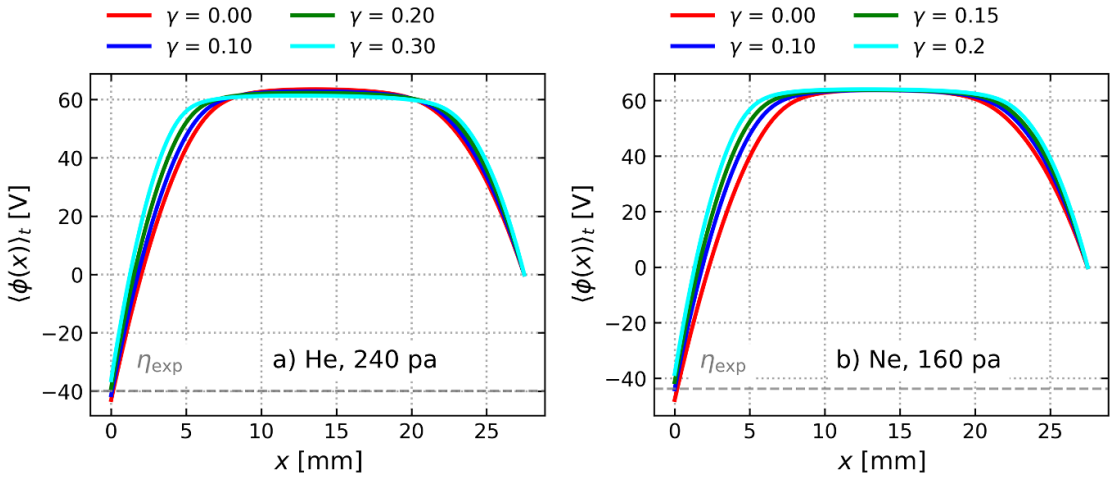


Figure 7. Spatial profiles of the time-averaged electrostatic potential $\langle\phi(x)\rangle_t$ for (a) He at 240 Pa and (b) Ne at 160 Pa for different values of γ. The horizontal dashed line in each panel indicates the experimentally measured DC self-bias voltage η ($\eta = -40.0$ V for He and $\eta = -43.8$ V for Ne). Discharge conditions: $f_1 = 4$ MHz, $\phi_1 = 160$ V, $\phi_2 = 80$ V, $L = 2.75$ cm, $R = 0.7$, and $\theta = 350°$.

4. Conclusion

In this study, we applied an *in-situ*, simulation-assisted method to determine the effective secondary electron emission coefficient, γ, for helium and neon in a CCP. The method is based on the sensitivity of the DC self-bias voltage η—which develops because of the EAE—to changes in γ under dual-frequency excitation.

We performed systematic PIC/MCC simulations for helium and neon under discharge conditions matching the experiments, and determined γ by comparing the computed DC self-bias with the experimentally measured values. For helium, effective γ values of 0.105 at 120 Pa and 0.165 at 240 Pa were obtained. For neon, we found $\gamma = 0.072$ at 80 Pa and $\gamma = 0.103$ at 160 Pa. The estimated uncertainty of the secondary emission coefficients is ± 0.01, as in [40].

In addition, we analyzed the underlying physical mechanisms responsible for the variation of DC self-bias voltage with γ. The simulations reveal that the increase in γ leads to enhanced ionization near the powered electrode due to more energetic secondary electrons. This effect increases the asymmetry of the plasma, which is reflected in the growing symmetry parameter ε, and explains the decrease of the DC self-bias voltage observed both in the simulations and in the model.

Our method provides a robust and practical approach for the *in-situ* determination of the effective SEEC in CCPs, without requiring complex optical diagnostics.

Acknowledgments

AD received support from the J Bolyai Scholarship of the Hungarian Academy of Sciences. (HAS). We thank Mate Vass for his help in analyzing the DC self-bias–γ dependence.

Data availability statement

The data cannot be made publicly available upon publication because they are not available in a format that is sufficiently accessible or reusable by other researchers. The data that support the findings of this study are available upon reasonable request from the authors.

Appendix

Table 4. Dependence of the DC self-bias voltage η at $\theta = 350°$ on γ, shown along with the symmetry parameter ε, and the corresponding peak sheath voltages, extracted from PIC/MCC simulations of helium at 120 Pa.

γ	η (V)	$\overline{n}_{sp}/\overline{n}_{sg}$	$(Q_{mg}/Q_{mp})^2$	ε	$\lvert\widehat{\phi}_{sp}\rvert$ (V)	$\widehat{\phi}_{sg}$(V)
0.00	−48.6	0.91	1.06	0.99	184.1	181.7
0.01	−48.5	0.92	1.07	0.99	183.9	181.8
0.10	−48.0	0.91	1.07	0.99	183.2	182.1
0.15	−47.8	0.91	1.08	1.00	182.8	182.4
0.20	−47.6	0.91	1.08	1.00	182.4	182.5
0.25	−47.0	0.90	1.09	1.01	181.7	183.2
0.30	−46.8	0.90	1.12	1.01	181.2	183.6

Table 5. Dependence of the DC self-bias voltage η at $\theta = 350°$ on γ, shown along with the symmetry parameter ε, and the corresponding peak sheath voltages, extracted from PIC/MCC simulations of helium at 240 Pa.

γ	η (V)	$\overline{n}_{sp}/\overline{n}_{sg}$	$(Q_{mg}/Q_{mp})^2$	ε	$\lvert\widehat{\phi}_{sp}\rvert$ (V)	$\widehat{\phi}_{sg}$ (V)
0.00	−43.0	0.97	1.04	1.04	175.4	182.6
0.01	−42.8	0.97	1.04	1.04	175.3	182.7
0.10	−41.4	0.99	1.05	1.06	173.6	184.2
0.15	−40.4	1.00	1.05	1.08	172.4	185.4
0.20	−39.0	1.01	1.07	1.09	171.2	186.9
0.25	−37.8	1.02	1.07	1.11	169.9	188.6
0.30	−36.2	1.03	1.09	1.13	168.5	190.8

Table 6. Dependence of the DC self-bias voltage η at $\theta = 350^\circ$ on γ, shown along with the symmetry parameter ε, and the corresponding peak sheath voltages, extracted from PIC/MCC simulations of neon at 80 Pa.

γ	η (V)	$\overline{n}_{sp}/\overline{n}_{sg}$	$(Q_{mg}/Q_{mp})^2$	ε	$\lvert\widehat{\phi}_{sp}\rvert$ (V)	$\widehat{\phi}_{sg}$ (V)
0.000	−48.3	0.92	1.07	1.01	188.8	190.9
0.050	−47.0	0.93	1.07	1.03	187.1	191.8
0.100	−45.5	0.95	1.06	1.04	185.2	192.8
0.125	−44.5	0.95	1.07	1.05	184.1	193.6
0.150	−43.7	0.96	1.07	1.06	183.0	194.2
0.175	−42.8	0.97	1.07	1.07	181.8	194.8
0.200	−41.8	0.98	1.07	1.08	180.6	195.7

Table 7. Dependence of the DC self-bias voltage η at $\theta = 350^\circ$ on γ, shown along with the symmetry parameter ε, and the corresponding peak sheath voltages, extracted from PIC/MCC simulations of neon at 160 Pa.

γ	η (V)	$\overline{n}_{sp}/\overline{n}_{sg}$	$(Q_{mg}/Q_{mp})^2$	ε	$\lvert\widehat{\phi}_{sp}\rvert$ (V)	$\widehat{\phi}_{sg}$ (V)
0.000	−47.8	0.95	1.05	1.02	187.0	190.2
0.050	−46.1	0.96	1.04	1.04	184.9	191.6
0.100	−44.0	0.99	1.04	1.06	182.6	193.4
0.125	−42.7	1.00	1.04	1.07	181.2	194.5
0.150	−41.4	1.01	1.03	1.09	179.6	195.7
0.175	−40.1	1.02	1.04	1.10	178.3	196.7
0.200	−38.5	1.04	1.04	1.12	176.6	198.2

ORCID iDs

Ranna Masheyeva 0000-0002-6950-662X
Aranka Derzsi 0000-0002-8005-5348
Karlygash Dzhumagulova 0000-0002-2937-4482
Murat Myrzaly 0000-0002-8811-7099
Zoltán Donkó 0000-0003-1369-6150
Peter Hartmann 0000-0003-3572-1310

References

[1] Lieberman M A and Lichtenberg A J 2005 *Principles of Plasma Discharges and Materials Processing* 2nd edn (Wiley) (https://doi.org/10.1002/0471724254)
[2] Makabe T and Petrovic Z L 2006 *Plasma Electronics: Applications in Microelectronic Device Fabrication* 1st edn (CRC Press) p 360
[3] Donnelly V M and Kornblit A 2013 Plasma etching: yesterday, today and tomorrow *J. Vac. Sci. Technol. A* **31** 050825
[4] Chang J P and Coburn J W 2003 Plasma-surface interactions *J. Vac. Sci. Technol. A* **21** S145–51
[5] Xia D, Zhu X, Khanom F and Runt D 2020 Neon and helium focused ion beam etching of resist patterns *Nanotechnology* **31** 475301
[6] Livengood R, Tan S, Greenzweig Y, Notte J and McVey S 2009 Subsurface damage from helium ions as a function of dose, beam energy and dose rate *J. Vac. Sci. Technol. B* **27** 3244–9
[7] Gonzalez C M *et al* 2014 Focused helium and neon ion beam induced etching for advanced extreme ultraviolet lithography mask repair *J. Vac. Sci. Technol. B* **32** 021602
[8] Park Y C, Johnson N M, Jackson W B, Stevens K S, Smith D L and Hagstrom S B 1992 Effect of helium dilution during plasma-enhanced deposition on electron trapping in silicon dioxide thin films *Appl. Phys. Lett.* **60** 695–7
[9] Bartnik A, Wachulak P, Fiedorowicz H, Jarocki R, Kostecki J and Szczurek M 2013 Luminescence of he and ne gases induced by EUV pulses from a laser plasma source *Radiat. Phys. Chem.* **93** 9–13
[10] Little P F 1956 *Secondary Effects* vol 4/21 (Springer) 574–662
[11] Phelps A V and Petrovic Z L 1999 Cold-cathode discharges and breakdown in argon: surface and gas phase production of secondary electrons *Plasma Sources Sci. Technol.* **8** R21
[12] Dekker A 1958 Secondary electron emission *Solid State Physics* (*Solid State Physics: Advances in Research and Applications*) vol 6, ed F Seitz and D Turnbull (Academic) pp 251–311
[13] Hachenberg O and Brauer W 1959 Secondary electron emission from solids *Advances in Electronics and Electron Physics* vol 11, ed L Marton and C Marton (Academic) pp 413–99
[14] Belenguer P and Boeuf J P 1990 Transition between different regimes of RF glow discharges *Phys. Rev. A* **41** 4447–59
[15] Wen D Q, Krek J, Gudmundsson J T, Kawamura E, Lieberman M A, Zhang P and Verboncoeur J P 2023 On the importance of excited state species in low pressure capacitively coupled plasma argon discharges *Plasma Sources Sci. Technol.* **32** 064001
[16] Wen D Q, Krek J, Gudmundsson J T, Kawamura E, Lieberman M A and Verboncoeur J P 2021 Benchmarked and upgraded particle-in-cell simulations of a capacitive argon discharge at intermediate pressure: the role of metastable atoms *Plasma Sources Sci. Technol.* **30** 105009
[17] Radmilović-Radjenović M, Petrović Z L and Radjenović B 2007 Modelling of breakdown behavior by PIC/MCC code with improved secondary emission models *J. Phys.: Conf. Ser.* **71** 012007

[18] Radmilović-Radjenović M and Lee J K 2005 Modeling of breakdown behavior in radio-frequency argon discharges with improved secondary emission model *Phys. Plasmas* **12** 063501
[19] Braginsky O, Kovalev A, Lopaev D, Proshina O, Rakhimova T, Vasilieva A, Voloshin D and Zyryanov S 2011 Experimental and theoretical study of dynamic effects in low-frequency capacitively coupled discharges *J. Phys. D: Appl. Phys.* **45** 015201
[20] Gudmundsson J T, Krek J, Wen D Q, Kawamura E and Lieberman M A 2022 Surface effects in a capacitive argon discharge in the intermediate pressure regime *Plasma Sources Sci. Technol.* **30** 125011
[21] Liu Q, Liu Y, Samir T and Ma Z 2014 Numerical study of effect of secondary electron emission on discharge characteristics in low pressure capacitive RF argon discharge *Phys. Plasmas* **21** 083511
[22] Proto A and Gudmundsson J T 2018 The influence of secondary electron emission and electron reflection on a capacitively coupled oxygen discharge *Atoms* **6** 65
[23] Zhou Y, Zhao K, Ma F F, Sun J Y, Liu Y X, Gao F, Zhang Y R and Wang Y N 2025 Experimental and modeling investigation on charged particle dynamics and electron power absorption mode in 400 kHz/27.2 MHz dual-frequency capacitively coupled argon discharges *Plasma Sources Sci. Technol.* **34** 035016
[24] Park H and Lee H J 2025 Two-dimensional particle-in-cell simulation to investigate electron heating mechanism in intermediate-pressure RF hollow cathode discharges *Plasma Sources Sci. Technol.* **34** 035002
[25] Huang C, Shannon S C and Kushner M J 2025 Investigation of the effects of charging and secondary electron emission on high aspect ratio ONO plasma etching *Proc. Int. Symp. on Plasma Chemistry (ISPC)*
[26] Gopinath V P, Verboncoeur J P and Birdsall C K 1998 Multipactor electron discharge physics using an improved secondary emission model *Phys. Plasmas* **5** 1535–40
[27] Sun J Y, Wen D Q, Zhang Q Z, Liu Y X and Wang Y N 2019 The effects of electron surface interactions in geometrically symmetric capacitive RF plasmas in the presence of different electrode surface materials *Plasma Phys.* **26** 063505
[28] Sun G Y, Li Y, Zhang S, Song B P, Mu H B, Guo B H, Sun A B and Zhang G J 2019 Integrated modeling of plasma-dielectric interaction: kinetic boundary effects *Plasma Sources Sci. Technol.* **28** 055001
[29] Sun G Y, Guo B H, Mu H B, Song B P, Zhou R D, Zhang S and Zhang G J 2018 Flashover strength improvement and multipactor suppression in vacuum using surface charge pre-conditioning on insulator *J. Appl. Phys.* **124** 134102
[30] Wen D Q, Zhang P, Krek J, Fu Y and Verboncoeur J P 2022 Higher harmonics in multipactor induced plasma ionization breakdown near a dielectric surface *Phys. Rev. Lett.* **129** 045001
[31] Hofer W O 1990 Ion-induced electron emission from solids *Scanning Microscopy Supplement* vol 4 pp 265–310
[32] Baragiola R, Alonso E, Ferron J and Oliva-Florio A 1979 Ion-induced electron emission from clean metals *Surf. Sci.* **90** 240–55
[33] Hagstrum H D 1954 Auger ejection of electrons from tungsten by noble gas ions *Phys. Rev.* **96** 325–35
[34] Kim H K, Kim T S, Lee J and Jo S K 2007 Threshold behavior in kinetic electron emission from oxide insulators *Phys. Rev. B* **76** 165434
[35] Buschhaus R, Prenzel M and von Keudell A 2022 Ion-induced secondary electron emission of oxidized nickel and copper studied in beam experiments *Plasma Sources Sci. Technol.* **31** 025017
[36] Daksha M, Berger B, Schuengel E, Korolov I, Derzsi A, Koepke M, Donkó Z and Schulze J 2016 A computationally assisted spectroscopic technique to measure secondary electron emission coefficients in radio frequency plasmas *J. Phys. D: Appl. Phys.* **49** 234001
[37] Schulenberg D A, Korolov I, Donkó Z, Derzsi A and Schulze J 2021 Multi-diagnostic experimental validation of 1d3v pic/mcc simulations of low pressure capacitive RF plasmas operated in argon *Plasma Sources Sci. Technol.* **30** 105003
[38] Schulze C, Donkó Z and Benedikt J 2022 A computationally assisted technique to measure material-specific surface coefficients in capacitively coupled plasmas based on characteristics of the ion flux-energy distribution function *Plasma Sources Sci. Technol.* **31** 105017
[39] Beckfeld F, Masheyeva R, Derzsi A, Schulenberg D A, Korolov I, Bock C, Schulze J and Donkó Z 2025 Effective secondary electron yields for different surface materials in capacitively coupled plasmas *Plasma Sources Sci. Technol.* **34** 035009
[40] Masheyeva R, Hartmann P, Luo L Y, Dzhumagulova K, Liu Y X, Schulze J and Donkó Z 2024 On the in-situ determination of the effective secondary electron emission coefficient in low pressure capacitively coupled radio frequency discharges based on the electrical asymmetry effect *J. Phys. D: Appl. Phys.* **58** 045208
[41] Masheyeva R U, Dzhumagulova K N, Myrzaly M, Schulze J and Donkó Z 2021 Self-bias voltage formation and charged particle dynamics in multi-frequency capacitively coupled plasmas *AIP Adv.* **11** 075024
[42] Heil B G, Czarnetzki U, Brinkmann R P and Mussenbrock T 2008 On the possibility of making a geometrically symmetric RF-CCP discharge electrically asymmetric *J. Phys. D: Appl. Phys.* **41** 165202
[43] Lafleur T and Booth J P 2013 Frequency dependence of the electrical asymmetry effect in dual-frequency capacitively coupled discharges *Appl. Phys. Lett.* **102** 154104
[44] Lafleur T 2015 Tailored-waveform excitation of capacitively coupled plasmas and the electrical asymmetry effect *Plasma Sources Sci. Technol.* **25** 013001
[45] Sun J Y, Zhang Q Z, Liu J R, Song Y H and Wang Y N 2020 Electrical asymmetry effect in inhomogeneously magnetized capacitively coupled plasmas *Plasma Sources Sci. Technol.* **29** 114002
[46] Schulze J, Schüngel E, Donkó Z and Czarnetzki U 2011 The electrical asymmetry effect in multi-frequency capacitively coupled radio frequency discharges *Plasma Sources Sci. Technol.* **20** 015017
[47] Gudmundsson J T, Kawamura E and Lieberman M A 2013 A benchmark study of a capacitively coupled oxygen discharge of the oopd1 particle-in-cell Monte Carlo code *Plasma Sources Sci. Technol.* **22** 035011
[48] Birdsall C 1991 Particle-in-cell charged-particle simulations, plus Monte Carlo collisions with neutral atoms, pic-mcc *IEEE Trans. Plasma Sci.* **19** 65–85
[49] Matyash K, Schneider R, Taccogna F, Hatayama A, Longo S, Capitelli M, Tskhakaya D and Bronold F X 2007 Particle in cell simulation of low temperature laboratory plasmas *Contrib. Plasma Phys.* **47** 595–634
[50] Sun A, Becker M M and Loffhagen D 2016 PIC/MCC simulation of capacitively coupled discharges: effect of particle management and integration *Comput. Phys. Commun.* **206** 35–44
[51] Horváth B, Derzsi A, Schulze J, Korolov I, Hartmann P and Donkó Z 2020 Experimental and kinetic simulation study of electron power absorption mode transitions in capacitive radiofrequency discharges in neon *Plasma Sources Sci. Technol.* **29** 055002
[52] Biagi-v8.9 2010 Cross sections extracted from PROGRAM MAGBOLTZ, VERSION 8.9 (available at: www.lxcat.net/) (Accessed 25 November 2014)
[53] Pitchford L C *et al* 2017 LXCat: an open-access, web-based platform for data needed for modeling low temperature plasmas *Plasma Process. Polym.* **14** 1600098

[54] Phelps A V personal communication
[55] Verboncoeur J P 2005 Particle simulation of plasmas: review and advances *Plasma Phys. Control. Fusion* **47** A231
[56] Lymberopoulos D P and Economou D J 1995 Two-dimensional self-consistent radio frequency plasma simulations relevant to the gaseous electronics conference RF reference cell *J. Res. Natl Inst. Stand. Technol.* **100** 473
[57] Kim H C, Iza F, Yang S S, Radmilović-Radjenović M and Lee J K 2005 Particle and fluid simulations of low-temperature plasma discharges: benchmarks and kinetic effects *J. Phys. D: Appl. Phys.* **38** R283
[58] Vahedi V and Surendra M 1995 A monte carlo collision model for the particle-in-cell method: applications to argon and oxygen discharges *Comput. Phys. Commun.* **87** 179–98
[59] Demidov V I, Adams S F, Kaganovich I D, Koepke M E and Kurlyandskaya I P 2015 Measurements of low-energy electron reflection at a plasma boundary *Phys. Plasmas* **22** 104501
[60] Daksha M, Derzsi A, Mujahid Z, Schulenberg D, Berger B, Donkó Z and Schulze J 2019 Material dependent modeling of secondary electron emission coefficients and its effects on PIC/MCC simulation results of capacitive RF plasmas *Plasma Sources Sci. Technol.* **28** 034002
[61] Takeishi Y and Hagstrum H D 1965 Auger-type electron ejection from the (111) face of nickel by slow He^+, Ne^+ and Ar^+ ions *Phys. Rev.* **137** A641–7
[62] Vance D W 1967 Auger electron emission from clean and carbon-contaminated mo *Phys. Rev.* **164** 372–80
[63] Hagstrum H D 1953 Electron ejection from ta by He^+, He^{++} and He_2^+ *Phys. Rev.* **91** 543–51
[64] Varney R N 1954 Liberation of electrons by positive-ion impact on the cathode of a pulsed townsend discharge tube *Phys. Rev.* **93** 1156–60
[65] Arifov U A 1969 *Interaction of Atomic Particles With a Solid Surface/Vzaimodeistvie Atomnykh Chastits S Poverkhnost'yu Tverdogo Tela* 1st edn (Springer New York)
[66] Töglhofer K, Aumayr F and Winter H 1993 Ion-induced electron emission from metal surfaces—insights from the emission statistics *Surf. Sci.* **281** 143–52
[67] Lakits G, Arnau A and Winter H 1990 Slow-particle-induced kinetic electron emission from a clean metal surface: a comparison for neutral and ionized projectiles *Phys. Rev. B* **42** 15–24
[68] Pamperin M, Bronold F X and Fehske H 2018 Ion-induced secondary electron emission from metal surfaces *Plasma Sources Sci. Technol.* **27** 084003
[69] Mueller H, Hausmann R, Brenten H, Niehaus A and Kempter V 1993 Electron emission in collisions of slow rare gas ions with partially cesiated W(110) *Z. Phys. D* **28** 109–18
[70] Mahadevan P, Layton J K and Medved D B 1963 Secondary electron emission from clean surface of molybdenum due to low-energy noble gas ions *Phys. Rev.* **129** 79–83
[71] Czarnetzki U, Heil B G, Schulze J, Donkó Z, Mussenbrock T and Brinkmann R P 2009 The electrical asymmetry effect - a novel and simple method for separate control of ion energy and flux in capacitively coupled RF discharges *J. Phys.: Conf. Ser.* **162** 012010
[72] Brinkmann R P 2007 Beyond the step model: approximate expressions for the field in the plasma boundary sheath *J. Appl. Phys.* **102** 093303